

Characterization of hydrogel-scaffold mechanical properties and microstructure by using synchrotron propagation-based imaging

Naitao Li ^a, Xiaoman Duan ^a, Xiao Fan Ding ^a, Ning Zhu ^{a,b,c,*}, Xiongbiao Chen ^{a,d,**}

^a Division of Biomedical Engineering, College of Engineering, University of Saskatchewan, Saskatoon, SK, S7N 5A9, Canada

^b Canadian Light Source, Saskatoon, S7N 2V3, SK, Canada

^c Department of Chemical and Biological Engineering, College of Engineering, University of Saskatchewan, Saskatoon, SK, S7N 5A9, Canada

^d Department of Mechanical Engineering, College of Engineering, University of Saskatchewan, Saskatoon, SK, S7N 5A9, Canada

ARTICLE INFO

Keywords:

Tissue engineering
Hydrogel scaffolds
3D-printing
Mechanical characterization
Propagation-based imaging

ABSTRACT

Hydrogel-based scaffolds have been widely used in soft tissue regeneration due to their biocompatible and tissue-like environment for maintaining cellular functions and tissue regeneration. Understanding the mechanical properties and internal microstructure of hydrogel-based scaffold, once implanted, is imperative in tissue engineering applications and longitudinal studies. Notably, this has been challenging to date as various conventional characterization methods by, for example, mechanical testing (for mechanical properties) and microscope (for internal microstructure) are destructive as they require removing scaffolds from the implantation site and processing samples for characterization. Synchrotron radiation propagation-based imaging-computed tomography (SR-PBI-CT) is feasible and promising for non-destructive visualizing of hydrogel scaffolds. As inspired, this study aimed to perform a study on the characterization of mechanical properties and microstructure of hydrogel scaffolds based on the SR-PBI-CT.

In this study, hydrogel biomaterial inks composed of 3% w/v alginate and 1% w/v gelatin were printed to form scaffolds, with some scaffolds being degraded over 3 days. Both degraded and undegraded scaffolds underwent compressive testing, with the strains being controlled at the preset values; meanwhile stresses within scaffolds were measuring, resulting the stress-strain curves. Concurrently, the scaffolds were also imaged and examined by SR-PBI-CT at Canadian Light Source (CLS). During the imaging process, the scaffolds were mechanically loaded, respectively, with the strains same as the ones in the aforementioned compressive testing, and at each strain, the scaffold was scanned with a pixel size of 13 μm .

From the stress-strain curves obtained in the compression testing, the Young's modulus was evaluated to characterize the elastic behavior of scaffolds: with the range between around 5–25 kPa. From the images captured by SR-PBI-CT, the scaffolds' microstructures were examined in terms of the strand cross-section area, pore size, and hydrogel volume. Further, from the SR-PBI-CT images, the stress within hydrogel of scaffolds were evaluated, showing the agreement with those obtained from compression testing. These results have illustrated that the mechanical properties and microstructures of scaffolds, either being degraded or not, can be examined and characterized by the SR-PBI-CT imaging, in a non-destructive manner. This would represent a significant advance for facilitating longitudinal studies on the scaffolds once implanted *in-vivo*.

1. Introduction

Porous scaffolds play a key role in tissue engineering aimed at treating damaged tissue or organs. The scaffolds provide the essential structure and microenvironment that support cellular adhesion,

proliferation, and differentiation, all of which are critical for tissue growth and maturation (Hollister, 2005). These scaffolds must be biodegradable, to allow the regeneration of new tissue as the scaffolds degrade (Loh and Choong, 2013). Different materials, such as bioceramics, biodegradable polymers, and hydrogel materials, are used to

* Corresponding author. Division of Biomedical Engineering, College of Engineering, University of Saskatchewan, Saskatoon, SK S7N 5A9, Canada

** Corresponding author. Division of Biomedical Engineering, College of Engineering, University of Saskatchewan, Saskatoon, SK, S7N 5A9, Canada

E-mail addresses: naitao.li@usask.ca (N. Li), xid896@mail.usask.ca (X. Duan), xid454@mail.usask.ca (X.F. Ding), ning.zhu@lightsource.ca (N. Zhu), xbc719@mail.usask.ca (X. Chen).

fabricate these scaffolds (Ma, 2004). The typical process of applying scaffolds for treating damaged tissue/organs (Chen, 2019) is shown in Fig. 1, which includes the following steps: selection of appropriate growth factors, cells/stem cells, and biomolecules, scaffold fabrication, culturing and implantation of scaffold to the body/test animal.

Hydrogel-based biomaterials have been widely used in the fabrication of scaffolds for soft tissue regeneration due to their superiority in providing a biocompatible, tissue-like environment for maintaining cellular functions and tissue regeneration. Hydrogel materials are able to mimic the natural extracellular matrix (ECM) with high water content and porosity (Hennink and van Nostrum, 2012), appropriate mechanical properties for scaffold support, and biological properties for cell (Chen, 2019; Tibbitt and Anseth, 2009; Singh et al., 2015; Zhang and Khademhosseini, 2017). Despite the popularity of hydrogel-based scaffolds, they are limited by their inherent mechanical weakness and structure instability (Radulescu et al., 2022; Saroia et al., 2018; Naahidi et al., 2017). As such, understanding the mechanical properties and behaviors of hydrogel-based scaffolds, particularly after implantation, becomes imperative in tissue engineering applications and longitudinal studies.

Hydrogel scaffolds typically have limited mechanical strength for maintaining the proper support for tissue regeneration (Naghieh et al., 2018a). Various studies have indicated that the mechanical properties of hydrogel scaffolds, such as their compressive strength and elastic modulus, are typically lower than those of native tissues (Tibbitt and Anseth, 2009; Gong, 2010). This discrepancy poses a significant challenge to their application in tissue engineering, especially when sufficient mechanical strength is crucial.

Usually, scaffolds are expected to simulate the mechanical performance of target tissue, and the requirements on the different applications of scaffolds are expected to be consistent with target tissue (Naghieh et al., 2018b). The most notable difference in mechanical properties among various types of tissues and tissue scaffolds lies in their elastic modulus (Handorf et al., 2015). Fig. 2 depicted the elastic modulus of various tissues. Typically, the elastic modulus of soft tissues falls within the range of 1–100 kPa, while hard tissues typically exhibit a significantly higher modulus, exceeding 1000 kPa (Lei et al., 2021; Cox and Erler, 2011).

Mechanical property characterization of tissue scaffolds is important for the development of scaffolds for tissue regeneration, and it is critical to characterize both mechanical properties and internal microstructure of scaffolds (Chen, 2019). Tissue engineering scaffolds must be strong enough to maintain the designed structure, as the scaffold material degrades and new tissue regenerates (Shimojo et al., 2020; Jang et al., 2023/03; Zhao et al., 2018/03). The scaffold structure may also be changed by the forces produced by kinetic bodies, or unexpected external forces such as compression and stretching (Larson and Shepherd, 2016). Conventional approaches, such as compression, tensile, bending, and torsion, form a robust and comprehensive strategy to evaluate the mechanical properties of tissue engineering scaffolds (Discher et al., 2005; Derby, 2012; Martino et al., 2014; Lu and Thiomopoulos, 2013). Besides the mechanical loading tests, visualizing and assessing the scaffold microstructure, such as pore size and porosity, are also important and represent a critical aspect of tissue engineering, as

these attributes significantly influence mechanical properties (Karageorgiou and Kaplan, 2005; Zadpoor, 2019).

Unfortunately, the current large-depth visualization techniques cannot meet the requirements for visualizing soft hydrogel scaffolds. Micro-computed tomography (μ CT) and magnetic resonance imaging (MRI) are commonly used as 3D imaging methods that provide sufficient depth and resolution for life science studies such as scaffold visualization (Rawson et al., 2020; Cheah et al., 2003; Szulc et al., 2020). MRI is often constrained due to its insufficient resolution when running with acceptable scanning speed (Kim et al., 2024; Stucht et al., 2015). In contrast, μ CT is frequently favored in such studies, such as the examination of 3D polycaprolactone (PCL)-based scaffolds but with a longer scanning time up to several hours (Clark et al., 2020). Long scanning time is not suitable for studies involving soft tissues, since motion artifacts may be introduced into images due to the deformation during the scans (Metcalf et al., 2020). In addition to the aforementioned limitations, another critical challenge in conventional absorption-based μ CT is that it is impossible to visualize low-density materials, such as hydrogel, due to the low X-ray absorption attenuation of these materials (Ning et al., 2021; Duan et al., 2021).

By contrast, synchrotron radiation propagation-based imaging-computed tomography (SR-PBI-CT) is capable of visualization and characterization of hydrogel scaffolds and significantly advantageous compared to conventional μ CT (Duan et al., 2021). Synchrotron radiation is a brilliant light source producing X-rays of high photon flux and coherence, ensuring a more significant potential for the development of new imaging techniques. PBI is one of SR imaging techniques, based on the refraction of X-rays and has shown promise for soft tissue visualization due to much higher refractive index variations compared to X-ray absorption coefficient variations (Lewis, 2004). Because of the high brightness and high coherence of SR source, SR-PBI imaging has shown great capability to visualize and distinguish low-density soft tissues and hydrogels with high spatial resolution and scan speed (Izadifar et al., 2016).

In our previous work (Ning et al., 2021), preliminary imaging and analysis of internal structures under compression loading have been conducted, demonstrating the great feasibility of applying SR-PBI-CT on internal micro-structure visualization of hydrogel scaffolds, for both *in-virtual* and *in-vivo* visualization. Consequently, it is critical to develop a comprehensive mechanical characterization method that encompasses both mechanical properties and detailed micro-structure change analysis of scaffolds to facilitate the advancement of soft tissue engineering scaffolds.

2. Methods

2.1. Materials and methods for hydrogel scaffolds fabrication and degradation

2.1.1. Hydrogel preparation

Medium-viscosity alginate powder (A2033, Sigma) and gelatin powder (from porcine skin, G1890, Sigma) were exposed under UV light for 90 min for sterilization. The alginate and gelatin powders were thoroughly dissolved in phosphate-buffered saline (PBS) to prepare 3% alginate mixed with 1% (w/v) gelatin (hereafter Alg-Ge). All hydrogel solutions were prepared in a sterile environment and transferred to a 4 °C fridge and stored for no more than two weeks.

The detailed protocol for preparing 50 ml of Alg-Ge biomaterial ink is given below:

- 1) Mix 1.5 g alginate powder and 0.5 g gelatin powder with 50 ml distilled water in a beaker.
- 2) Place the beaker on a hot plate and stir overnight. The temperature of the hot plate was set at 60 °C and stir speed was set at 120 rpm.
- 3) Move the solution into a 37 °C incubator for 24 h to completely dissolve.

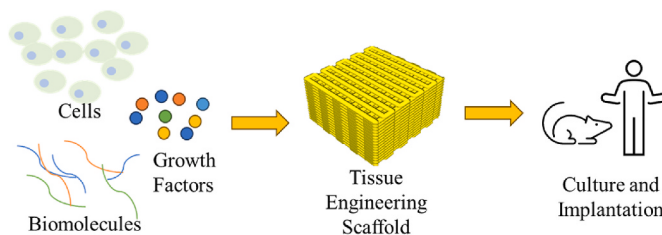


Fig. 1. Schematic depicting the schemes in tissue regeneration employing scaffolds.

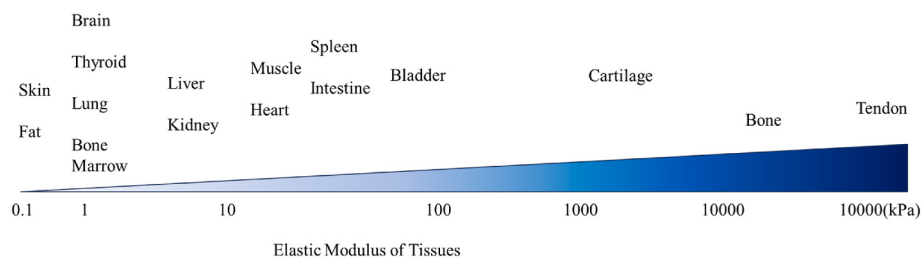


Fig. 2. Elastic modulus of different types of tissue.

- 4) Expose the biomaterial ink under UV light for 90 min for sterilization, then move the biomaterial ink into a 50 ml falcon tube for storage in a 4 °C fridge.
- 5) Expose the biomaterial ink under UV light for 90 min before printing.

2.1.2. Crosslinker preparation

Two kinds of crosslinkers were prepared for the subsequent printing process: One was prepared by dissolving 50 mM/L calcium chloride in 0.1% polyethylenimine (PEI; J61270, Alfa Aesar) solution and the other one by dissolving 100 mM/L calcium chloride in distilled water. All solutions were then exposed to UV light for 90 min for sterilization.

2.1.3. Hydrogel scaffolds design and fabrication

The scaffolds were designed in a cubic shape using Magic 13 Enviontec software, with a size of $10 \times 10 \times 5$ mm³. Then the cubic file was sliced with a layer height of 160 μ m, generated the project file for the control software of the Envision Bioplotter; and the inner structure design was done through the control software of the Envision Bioplotter (VisualMachine software). The infill pattern was the zigzag line and the angle difference between each layer is 90°. The strand distance in each layer is 1.25 mm. The schematic of designed scaffold is shown in Fig. 3.

Meanwhile, the printed bulks for following material stiffness assessment were also prepared using 3D printing, by changing strand distance to 0.65 mm and keeping all other parameters same. Printed bulks are solid filled hydrogel prints designed as test samples with the same shape as scaffolds but without internal pores. The strand distance of 0.65 mm was calculated based on the volume extrusion speed from imaging data of scaffolds.

The printing of Alg-Ge was carried out using a 3D bioprinter (Envision TEC, Inc., Germany), as shown in Fig. 4. Prepared hydrogels were, respectively, extruded with air pressures ranging from 10 to 60 kPa over defined time periods at 37 °C. Meanwhile, the movement speed of the printing head can be adjusted within a range of 1–30 mm/s. The printing parameters for Alg-Ge were carefully determined through numerous trials, and the optimal settings were found and applied during fabrication of scaffolds. Tapered needles with an inner diameter of 200 μ m at the outlet (gauge 27, Nordson EFD) were used. The temperature of the

printing head and bed were set at 37 °C.

Scaffolds were printed using the printing while cross-linking strategy, in which the hydrogel was extruded into the cross-linking medium, as shown in Fig. 5. Before printing, the well surface (12-well plate) was coated with 0.5% w/v polyethylenimine (PEI; J61270, Alfa Aesar) and incubated at 37 °C in an incubator for 24 h. After removing the PEI, the plates were rinsed with PBS and each well filled with 2.5 mL of calcium chloride solution, with a concentration of 50 mM/L. During the printing process, a constant printing pressure of 30 kPa was applied. The printing head speed was 18 mm/s for Alg-Ge. Five minutes after printing, printed scaffolds were removed from the bottom of well plates and the cross-linking medium was replaced with fresh calcium chloride solution (100 mM/L) and kept at 4 °C for 48 h to complete cross-linking.

2.1.4. In-vitro degradation of printed alginate-based hydrogel scaffolds

The samples were incubated in 10 mM/L PBS at 37 °C and 5% carbon dioxide for selected degradation periods. The crosslinker was taken out of the samples and the samples were rinsed by PBS, then samples were soaked in PBS and placed in 37 °C incubator. The ratio of PBS volume to each scaffold was 2 mL/scaffold.

The time point selection of degraded scaffolds in this study is critical for the demonstration of the mechanical characterization method. The use of crosslinking of only alginate in biomaterial ink can facilitate better control over degradation, particularly when compared to other content crosslinked (Luo et al., 2022). The degradation rate of the scaffold can be more precisely regulated when only the alginate is crosslinked. In this study, the scaffolds were considered as “degraded” at the 72-h mark. By this time point, degraded scaffolds had a significantly change on stiffness, meanwhile could keep the shape for the mechanical test and internal architecture imaging (see Fig. 6).

2.2. Stress-strain characterization of hydrogel scaffolds

2.2.1. Compression test set-up

Alg-Ge scaffolds with different degradation periods were tested using a compressive testing instrument (Biodynamic System, BOSE) for compression test. Unconfined compression was used for all tests, as

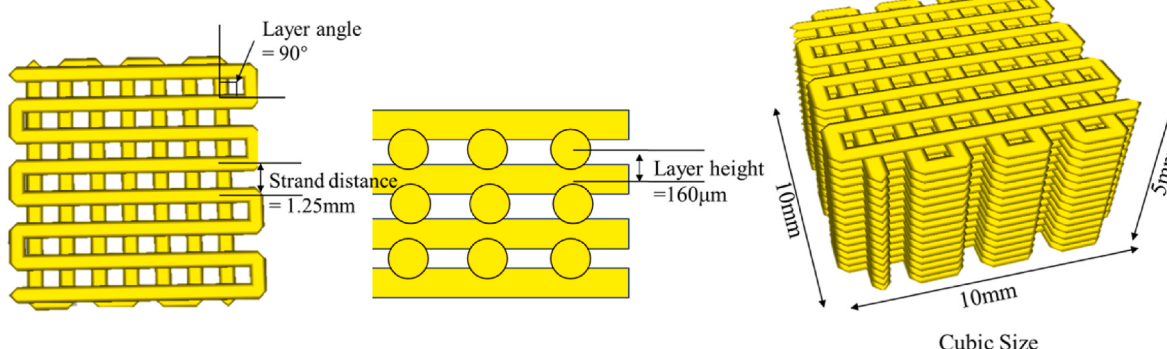


Fig. 3. Schematic of scaffold design.

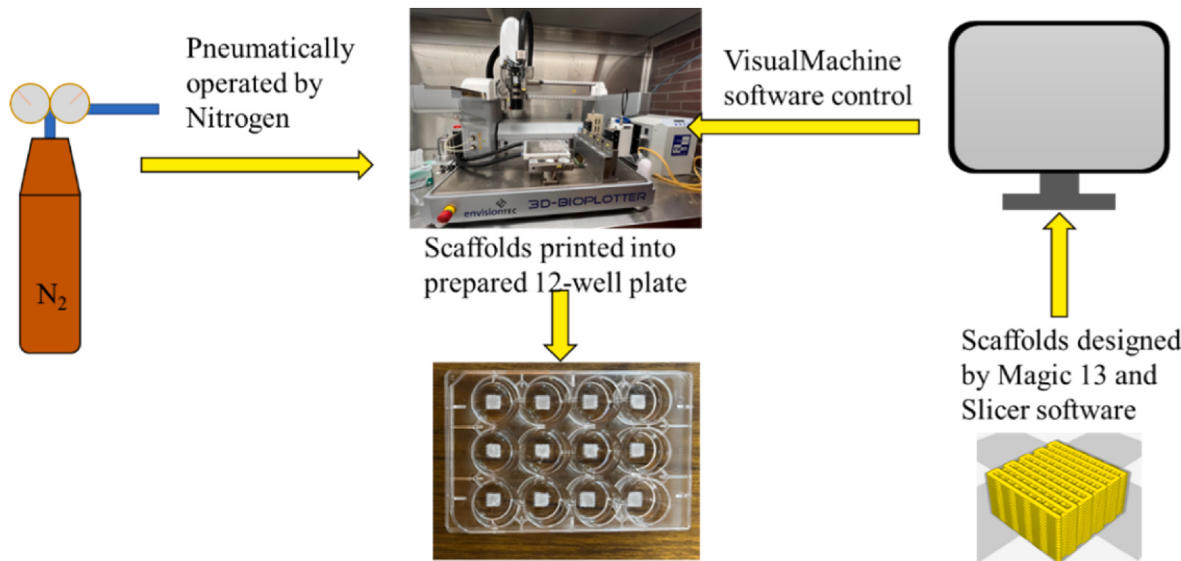


Fig. 4. Scaffold 3D printing set-up.

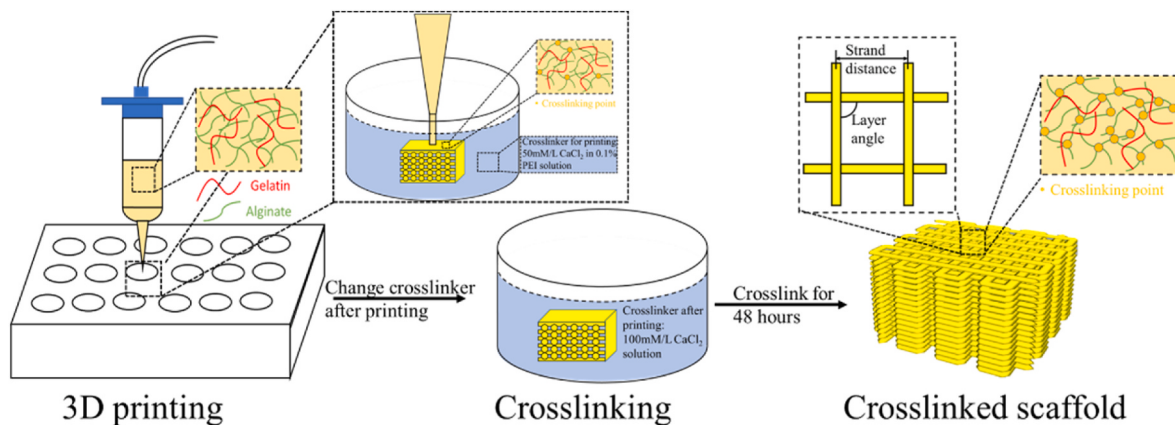


Fig. 5. Scaffold printing and crosslinking strategy.

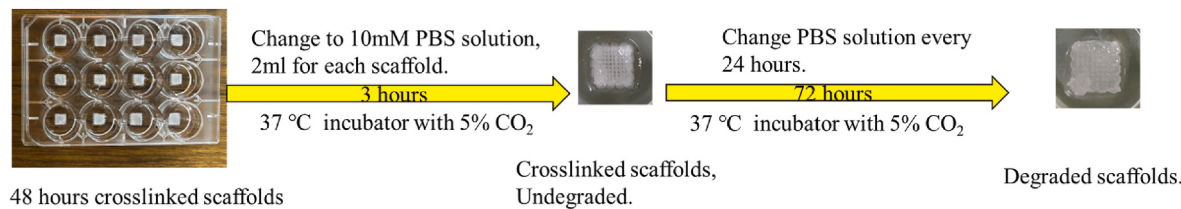


Fig. 6. In-vitro degradation experiments of scaffolds.

shown in Fig. 7. Before loading the scaffolds, the height of the scaffolds and the height after loading were measured by a caliper, with a resolution of 0.1 mm. The initial height of the scaffolds was measured to ensure the scaffolds were not compressed after loading the sample into the testing instrument, meanwhile, the readings from the force sensor were double-checked to ensure the scaffolds were correctly loaded. After loading each sample, the loaded sample was compressed with a modified loading strategy, as described in the following section. After testing, the testing time, compressive displacement, and compressive force of each sample during the test were recorded for stress-strain data processing.

2.2.2. Modified compressive loading

In this study, compression test was performed with a modified

compressive loading on the scaffolds, which was also used on the subsequent imaging of scaffolds. As illustrated Fig. 8, compressive loading was applied to the scaffold sample at a speed of 0.1 mm/s, to reach strains of 10%, 20%, 30%, 40%, and 50%, respectively. Upon reaching each of these strains, the displacement was held for 5 min, and the relaxing progress of the sample was recorded as the gradually reducing compressive force. The same loading conditions were also applied to the samples of scaffolds which were to be imaged by synchrotron, where during the period of 5 min, the imaging and data acquisition took place.

2.2.3. Stress-strain data processing

The compressive stress and modulus during imaging period for each group of scaffolds were calculated from the corresponding section of the

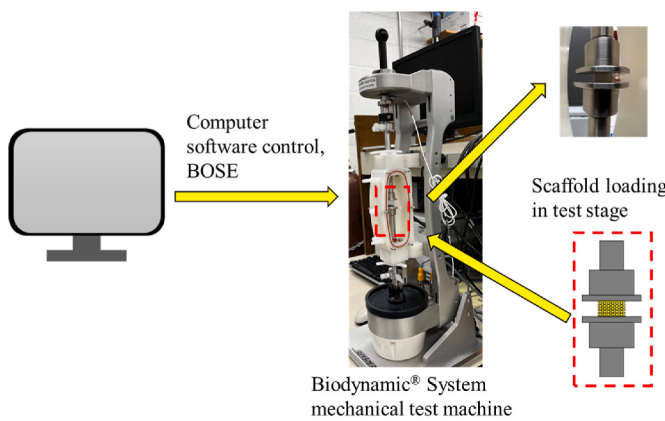


Fig. 7. Compression test set-up.

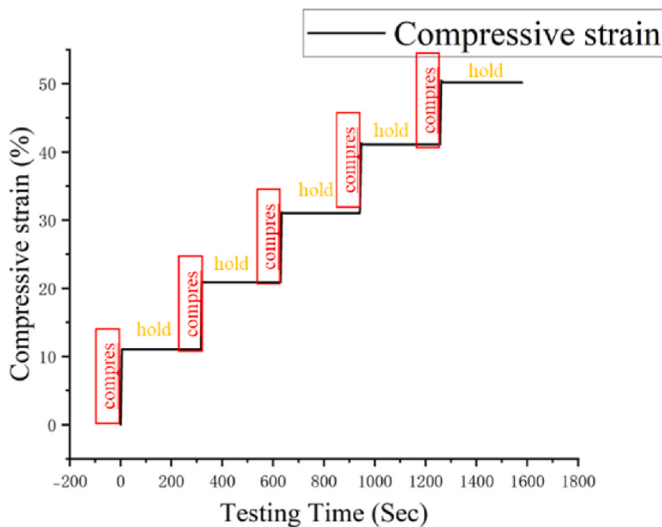


Fig. 8. Modified compressive strain-time loading plot.

stress-strain curve, which were obtained from the average value of four compression tests ($n = 4$) for both undegraded and degraded scaffolds. The detailed method of calculation is presented below.

- 1) Determine of relaxed compressive force. Relaxed compressive forces were determined with the average value of the force during the last 5 s of each "hold" phase of testing.
- 2) Calculation of cross-sectional area. Cross-sectional areas for mechanical properties calculation are measured differently in this research.

For scaffolds, there are designed and measured values. Designed value was used for evaluation of scaffolds without imaging data, which was designed outer dimensions; measured values were used for evaluating hydrogel in scaffolds, which were obtained from imaging data, by averaging the area values along the central 10% zone along the vertical direction of each scaffold.

For printed bulks, the cross-sectional area values were measured by conventional method: the length of edge was measured and recorded with a caliper, then side view photos were taken during compression, and edge length was continuously measured by photos. Then the area was calculated as a square, with measured length. The area calculated by this method should be slightly larger than the actual area since the corners of the printed bulk are rounded.

- 3) Calculation of stress and modulus. With compressive force and cross-sectional area, stress and modulus were calculated by their definition.

$$\text{Stress} = \frac{\text{Force}}{\text{Area}} \quad (2.1)$$

$$\text{Modulus} = \frac{\text{Stress}}{\text{Strain}} \quad (2.2)$$

2.3. Synchrotron radiation propagation-based imaging computed tomography (SR-PBI-CT) set-up and data processing

2.3.1. Development of synchrotron imaging compressive retention device

The study employed the PBI-CT technique to visually examine scaffolds that underwent different levels of compressive strains (Fig. 9). This technique provided highly accurate 3D data, allowing for a novel perspective that goes beyond traditional mechanical testing. But conventional mechanical test machine is not compatible with synchrotron imaging due to the strong absorption of X-ray beam caused by metal arm.

In order to ensure precise strain measurements, a specialized *in-vitro* X-ray compatible compressive retention device was developed using 3D printing. This device cannot contain metal components in beam and should be able to provide precise compression of hydrogel samples. The device featured a screw-driven piston controlled by a threaded fastener and buoyancy facilitated by PBS within the holder. Meanwhile the device was constructed with no metal material in imaging zone, which ensures the imaging quality of low-density hydrogel material. Precisely fitted square holder and piston ensure uniform compression and zero torsion. The scaffolds were subjected to continuous mechanical stimulation *in-vitro*, resulting in compressive deformation in this study.

2.3.2. SR-PBI-CT set-up

The PBI method was developed and performed at the 05ID-2 beamline at the biomedical imaging and therapy (BMIT) facility of the Canadian light source (CLS). Samples were imaged at 30 keV monochromatic X-ray beam and the sample-to-detector distance (SDD) set at 1.5 m. An indirect detection setup comprising of a Hamamatsu AA-60 beam monitor (Hamamatsu Photonics, Shizuoka, Japan) coupled with an ORCA Flash 4.0 camera (Hamamatsu Photonics, Shizuoka, Japan) with the pixel size of $13 \times 13 \mu\text{m}^2$. The imaging field of view is $26.6 \times 9.3 \text{ mm}^2$; 2000 projections were acquired over 180° rotation of the sample with an exposure time of 60 ms per projection. For each scaffold, an initial scan without the compression piston touching the scaffold was acquired, reconstructed, and measured to determine the required displacement of the piston to load the scaffold at 0% of strain level. Each scaffold ($n = 3$ for each group) was scanned at 0%, 10%, 20%, 30%, 40%, and 50% compressive strain, respectively, via the specifically designed and manufactured device (see Fig. 10).

2.3.3. Reconstruction, measurements, and segmentation of scanned data

Phase retrieval algorithms were applied to convert edge enhancement phase contrast to areal contrast for further quantitative analysis. An open-source package (the Ultra-Fast-Online, UFO) (Farago et al., 2022) was used to apply Paganin/homogeneous transport-of-intensity (TIE-Hom) phase retrieval algorithms (Paganin et al., 2002) on the projections, and CT reconstruction. The 3D volume rendering of the scaffolds was rebuilt with the entire block of the printed scaffolds using 3D Slicer. The following data processing involved 2D measurements and 3D volume segmentation analysis using ImageJ (Schneider et al., 2012), 3D slicer (Kikinis et al., 2014), Avizo 2021 (FEI Company) and Biomedisa (Lösel et al., 2020).

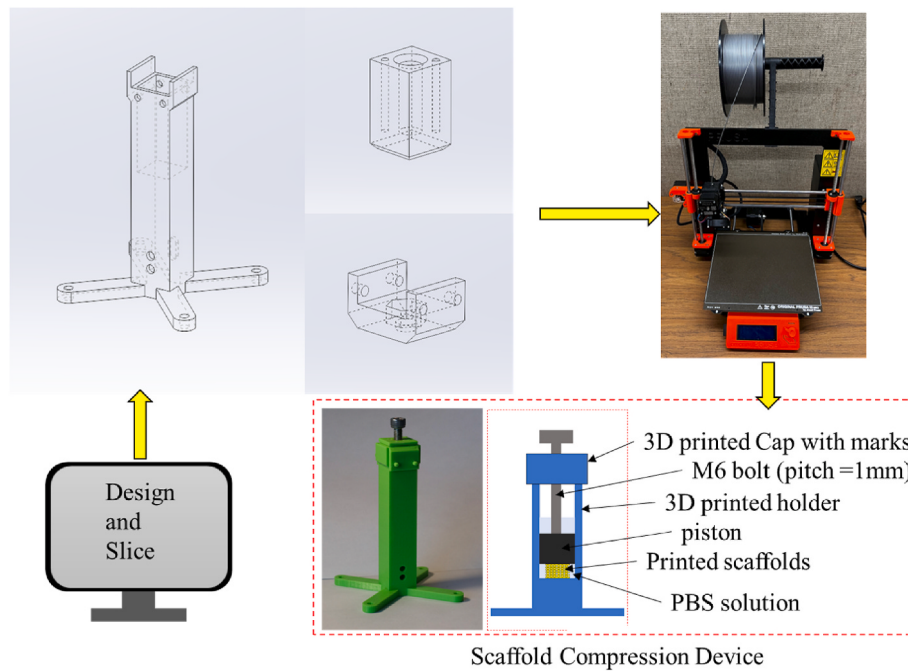


Fig. 9. Design and manufacture of synchrotron imaging compressive retention device.

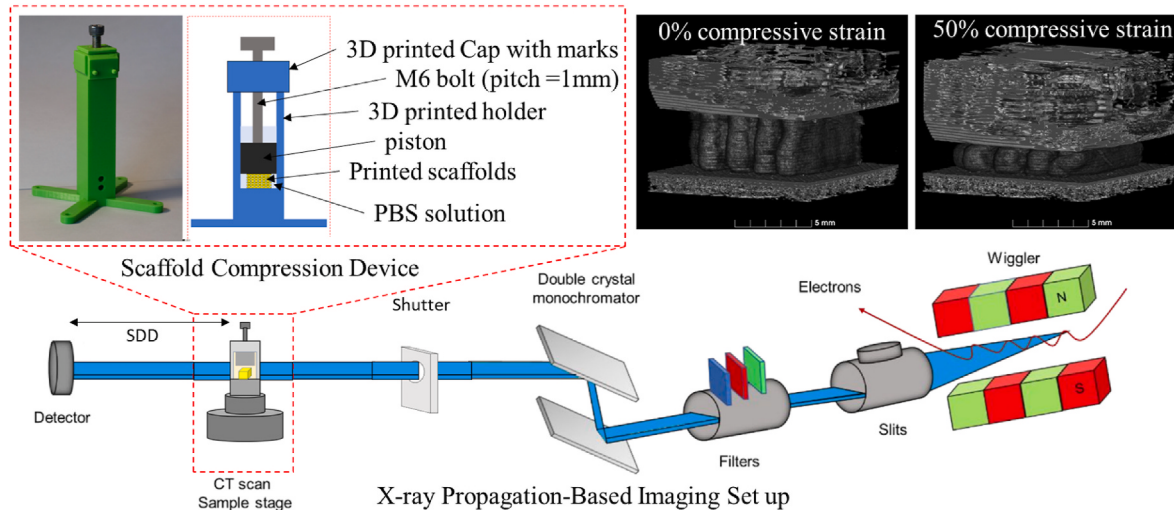


Fig. 10. SR-PBI-CT set-up.

2.3.4. Imaging data processing for structural and mechanical property assessment

The degraded and undegraded scaffolds were successfully scanned using the SR-PBI-CT setup, and reconstructed 3D imaging data were processed for mechanical assessment. After visual inspection, the changes on the architecture of scaffolds were quantified with precise 3D data. Firstly, the width, height, and cross-sectional area of strands were measured (see Fig. 11), by Image J. Then, the volume data and pore size and porosity of scaffolds were measured after volume segmentations done by segmenting around 10 slices in Avizo and interpolated through Biomedisa (see Fig. 12). The detailed flow of processing and calculation is presented below.

- Measurements of the width, height, and cross-sectional area of strands by Image J. Geometry properties of strand cross-sectional view were measured as the following figure, after setting scale with pixel size in Image J.

- Volume segmentation. The image dataset was first loaded into Avizo and several slices equidistant from each other were manually segmented. Then the pre-segmented labels were interpolated based on the underlying image data through Biomedisa which is a random-walk interpolation software. There are 3 parts segmented in the data, including hydrogel (blue), central pores (yellow), and outer pores (red).

- Calculation of hydrogel volume, porosity, and average pore size. First, segmented data was cropped and 10% height zone of scaffolds on both top and bottom was removed. Then the data was imported into 3D Slicer and the volume of 3 parts was obtained from software. Finally, values of the cross-sectional area of central pores were obtained in 3D slicer by percentage in height. Then, porosity and average pore size were calculated with the following equations:

$$\text{Porosity} = \frac{V_{\text{central pores}} + V_{\text{outer pores}}}{V_{\text{central pores}} + V_{\text{outer pores}} + V_{\text{hydrogel}}} \quad (2.3)$$

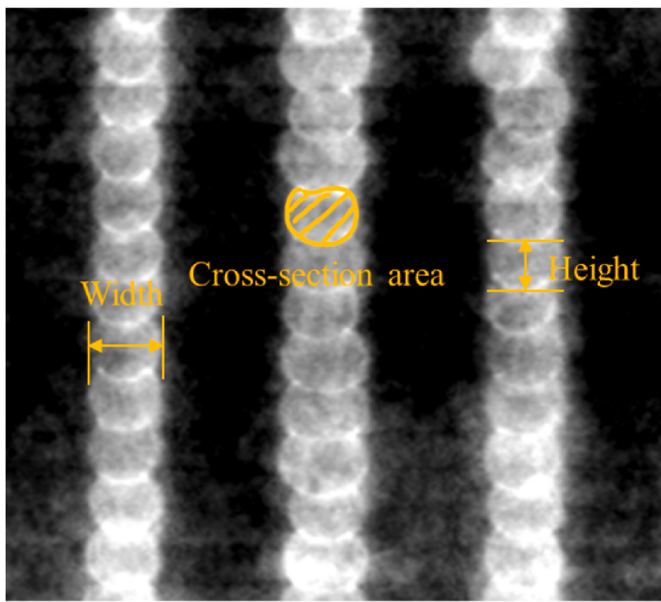


Fig. 11. Geometry measurements of strands in scaffolds.

$$\text{Average Pore Size} = \frac{\text{Average}(\text{Area}_{\text{central pores}})}{n}, n = 25. \quad (2.4)$$

2.4. Quantification and statistical analysis

All experiments were conducted in 3 repeats (for imaging results) or 4 repeats (for compression test) and the data were presented as the average value \pm standard deviation. Statistical analysis was conducted using one-way ANOVA on the results. P values < 0.05 were considered as statistically different and were marked in the plots using *.

3. Results and discussion

3.1. Compression tests on scaffolds

The applied stress was successfully determined with the compression test. The stress-time curves derived from the compression test revealed the typical viscoelastic behavior of hydrogel scaffolds as shown in Fig. 13b. Peaks in applied stress were observed during the compression phase of testing, whereas a gradual reduction in stress was evident during relaxation phase when maintaining the compressive strain. Stress values of scaffolds could be determined at any time point during the test, with the recorded stress-strain curve. In this research, the values of

relaxed stress were determined using average relaxed stress values recorded in the final 5 s of the imaging period. The stiffness of undegraded and degraded scaffolds were evaluated without imaging data by computing the relaxed Young's modulus at varying strains for each group. The degraded scaffolds exhibited distinct patterns compared to undegraded samples in the compression test. Specifically, degraded scaffolds displayed a higher modulus at lower compressive strains and softening at higher compressive strains (Fig. 13c). The compressive force applied, measured by simulating the mechanical environment of scaffolds during visualization, could serve as a reference of future mechanical analysis.

The elastic modulus of fabricated scaffolds was found to be similar to that of soft tissues and scaffolds with similar material from literatures. The undegraded scaffolds showed nonlinear elastic behavior, and the modulus ranged between around 5–25 kPa, which is within the range of soft tissues such as kidney, heart, muscle, and liver (Handorf et al., 2015; Lei et al., 2021). Moreover, these scaffolds showed a similar elastic modulus to the literature with similar alginate-based hydrogel scaffolds, such as 3% alginate scaffolds ranging from 15.47 to 32.1 kPa (Naghieh et al., 2018b), and 22 kPa for indirectly printed 3% alginate scaffolds (Naghieh et al., 2019a). Furthermore, for the printed scaffolds with the same Alg-Ge hydrogel material and similar structures, similar modulus and nonlinear elastic behavior from a previous publication were observed (Ning et al., 2021).

3.2. Fabrication and degradation of hydrogel scaffolds

Undegraded and degraded fabricated scaffolds with the same internal architecture were successfully prepared and imaged using the Alg-Ge solution. The geometric change caused by swelling and degradation was determined using precise 3D data. Firstly, volume rendering and slices from 2 perspectives were performed on undegraded and degraded scaffolds (Fig. 14b.). The reconstructed slices had sufficient image quality to distinguish the scaffold from its background, which indicated the feasibility of the SR-PBI-CT technique to visualize low-density hydrogel scaffolds. Imaging results showed that the scaffolds were printed following the designed pattern and strand distance. Then, the width, height, and cross-sectional area of strands were measured (Fig. 14c.). There was a significant increase in the width and cross-sectional area of the scaffolds with degradation and swelling. Meanwhile, there was almost no change in the height of strands. Finally, the volume data of scaffolds was measured after volume segmentations (Fig. 14d.). The volume of hydrogel in scaffolds increased, pore size and porosity decreased during degradation and swelling.

No lateral pore was observed in the printed scaffolds of this study. This is consistent with our previous research (Ning et al., 2021). The presence of lateral pores in scaffolds is related to the layer penetration of scaffolds. Layer penetration depends on biomaterial ink, structure

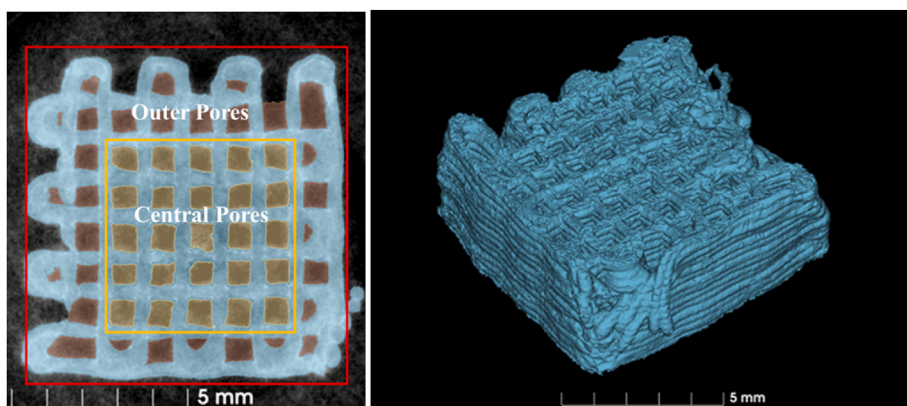


Fig. 12. Pre-segmentation, and segmented hydrogel of scaffolds.

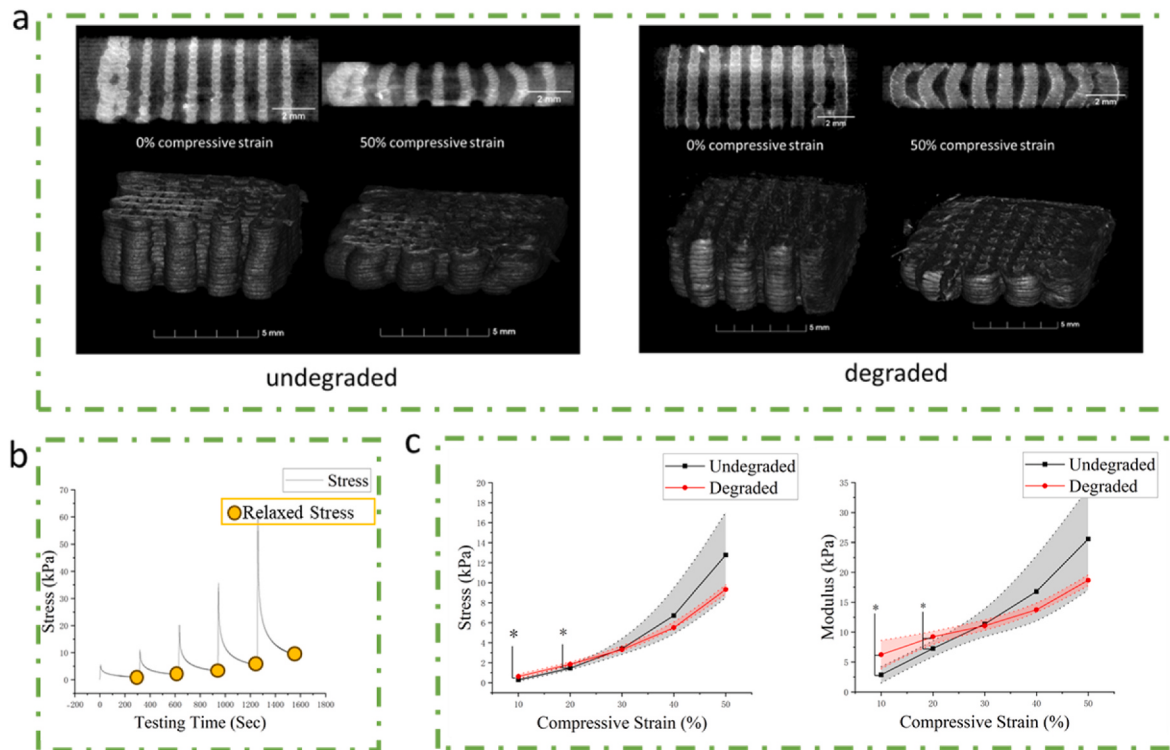


Fig. 13. Compression test of undegraded and degraded scaffolds. Volume rendering and longitudinal perspective of 2 groups of scaffolds before and after compression (a). Calculation strategy of relaxed stress. Sample of tested stress during compression test, with calculating zone of relaxed stress marked (b). Calculated stress and modulus of degraded and undegraded scaffolds, without imaging data ($n = 4$) (c). *, $p < 0.05$.

design, and can be affected by printing parameters as well (Naghieh et al., 2019b). Conversely, lateral pores can have an impact on the mechanical properties of the scaffold (Naghieh et al., 2018b). To simplify the change in mechanical performance by reducing structural differences after degradation and swelling, in this study, only scaffolds without lateral pores were used.

In this study, the selective crosslinking of only alginate in the biomaterial ink while leaving gelatin uncrosslinked, led to a faster degradation rate compared with all contents crosslinked (Luo et al., 2022). This is highly beneficial as it allows for a more comprehensive evaluation of multiple samples within a shorter timeframe. Additionally, this approach allows the use of scaffolds printed in the same batch, thereby reducing the impact of batch-to-batch differences. This is extremely advantageous as it ensures greater consistency and reliability in the experimental results.

3.3. SR-PBI-CT visualization and analysis of scaffolds under compressive strains

The stability of the structure was assessed by monitoring changes in the angle distribution of strands. This distribution was quantified based on positional shifts of the strands during compression (Fig. 15a). For this analysis, the base layer of strands was chosen as a reference. The angle distribution of subsequent layers relative to the base layer was then determined. During the compression process, the center of the scaffolds bulged outward, altering the overall angle distribution. This alteration was more pronounced in degraded scaffolds. Regarding the value of angle distribution change during compression, both the values and standard deviations of degraded scaffolds increased. This suggests a reduction in structure stability due to swelling and degradation.

Then, changes in the width, height, and cross-sectional area of the strands in both degraded and undegraded scaffolds during compression were measured and analyzed (Fig. 15b). All the data showed that as the width expanded, the cross-sectional area decreased during compression.

However, the height reduction of strands closely followed the compressive strain.

The pore size and porosity were then examined (Fig. 15c). Different segmentations based on precise CT reconstructed slices were generated to separate the hydrogel and pore, then the volume and cross-sectional area from the segmented reconstructed three-dimensional data were directly counted. During compression, there was a decline in porosity, pore size, and volume of hydrogel.

After measuring these deformations, values of strands cross-sectional area, average pore size and hydrogel volume during compression were normalized and depicted in Fig. 15d. The changes in strands cross-sectional area were consistent, but the degraded scaffolds showed a rapid decrease with increased compression. A more significant reduction was observed in average pore size, whereas the decrease in hydrogel volume was less pronounced during compression. In summary, degraded scaffolds exhibited a more substantial horizontal geometry shift, especially in strands cross-sectional area and average pore size. Conversely, the reduction in hydrogel volume in degraded scaffolds was relatively minor.

3.4. Analysis of the stress-strain curves based on SR-PBI-CT results

With the information from the scaffold images, the average stresses within the hydrogel of scaffolds (both with and without degradation) were evaluated. First, the compressive forces exerted during the compression were determined from the compression tests as described above, under the assumption that the forces applied to the scaffolds were identical given that the same loading conditions were applied to the scaffolds in both compression testing and imaging. Then, the cross-sectional area of the hydrogel was calculated, based on the imaging results, by averaging the area values within the central zone with a height of 10% of the entire scaffold height along the vertical direction. After that, the average stress values were derived from the above forces and cross-sectional area, with the result shown in Fig. 16a. On this basis,

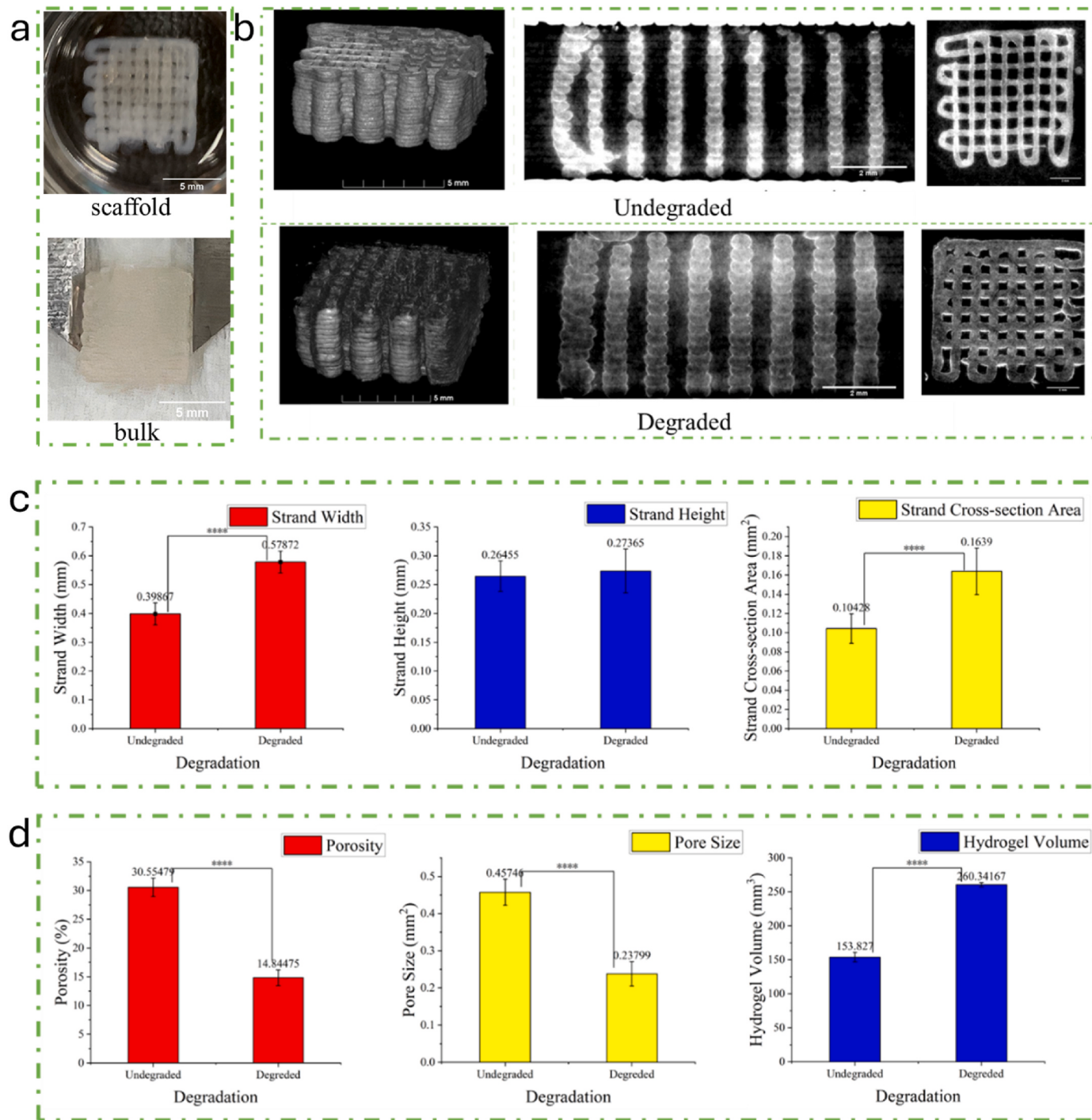


Fig. 14. Hydrogel scaffolds fabrication and visualization with degraded and undegraded samples. Photo of printed hydrogel scaffold and bulk, length of scalebars is 5 mm (a). Volume rendering and slices from 2 perspectives of undegraded and degraded scaffolds (b). Geometric change measurements of strands in undegraded and degraded scaffolds ($n = 3$ for each group), strands were randomly picked from 4 slices in 2 directions of longitudinal view of each scaffold, and 5 strands were randomly picked from each slice (c). Porosity, average pore size and hydrogel volume change during swelling and degradation ($n = 3$), counted with the 80% height range in the middle of the entire scaffolds (d). *, $p < 0.05$; **, $p < 0.01$; ***, $p < 0.005$; ****, $p < 0.0005$.

the module was also evaluated with the results presented in Fig. 16b. Both undegraded and degraded scaffolds exhibit a similar trend during compressive strain up to 30%, which is different from the result when the cross-sectional area is not considered (Fig. 16c). However, the stress within the hydrogel of undegraded scaffolds increases rapidly during compression. At 50% strain, the stress reached a significant difference between undegraded and degraded scaffolds, while the relaxed compressive forces were similar, respectively. The differences in

hydrogel stress are more pronounced than the variances in compressive force.

Meanwhile, the precision of this method is successfully verified with the comparison with the mechanical test results from a set of printed bulk samples. Relaxed stress and Young's modulus of hydrogel within undegraded scaffolds and printed bulks were similar (Fig. 16b), considering the cross-sectional area of bulk was calculated slightly larger compared with the actual area using the conventional measuring,

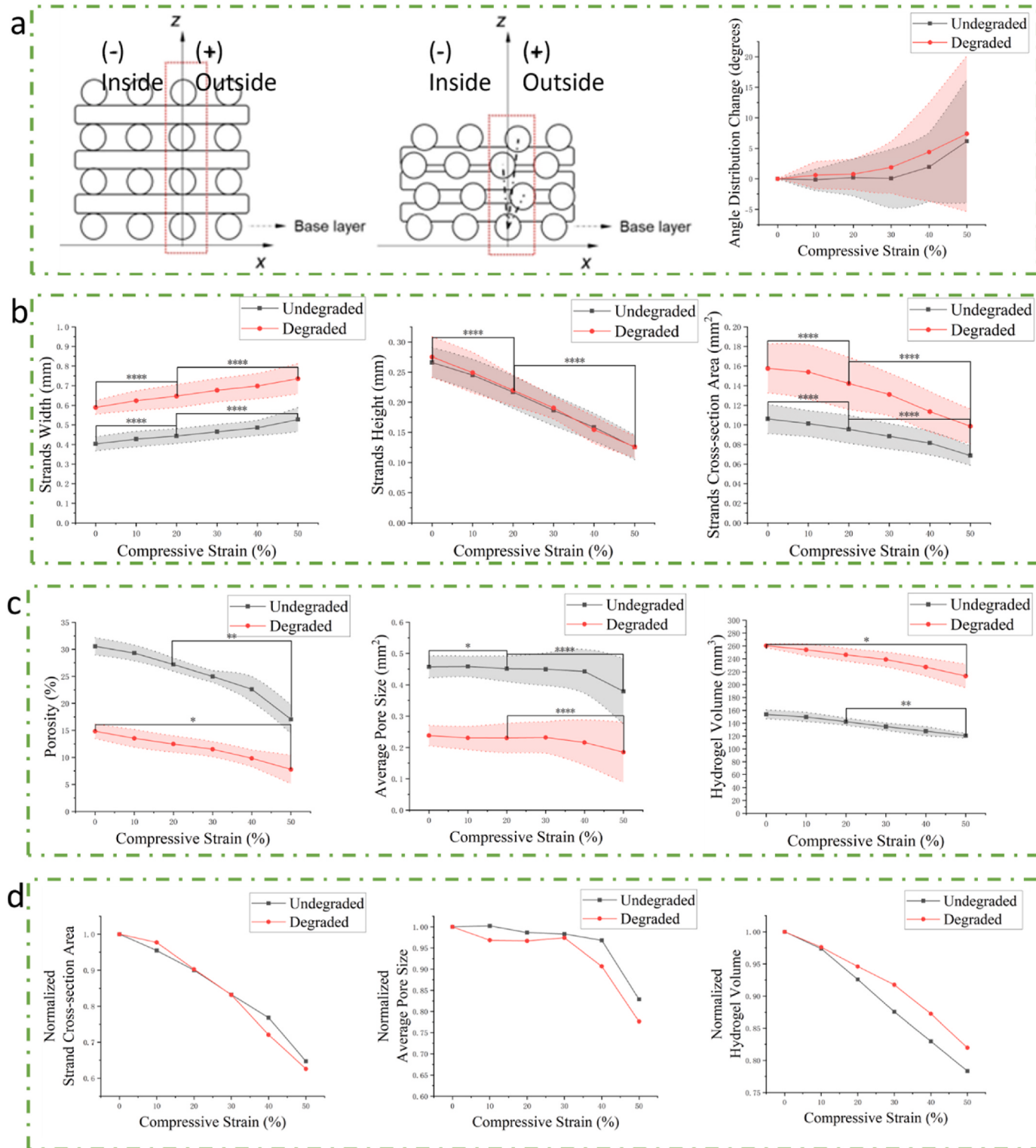


Fig. 15. PBI-CT visualization and analysis of scaffolds under different compressive strains. Measurement scheme and result of angle distribution change of undegraded and degraded scaffolds during compression (a). Geometric change measurements of strands in undegraded and degraded scaffolds ($n = 3$) during compression, strands were randomly picked from 4 slices in 2 directions of longitudinal view of each scaffold, and 5 strands were randomly picked from each slice (b). Porosity, average pore size and hydrogel volume change during compression of undegraded and degraded scaffolds ($n = 3$), statistics are made on the 80% height range in the middle of the scaffolds (c). Normalized strands cross-sectional area, average pore size, and hydrogel volume during compression (d). *, $p < 0.05$; **, $p < 0.01$; ***, $p < 0.005$; ****, $p < 0.0005$.

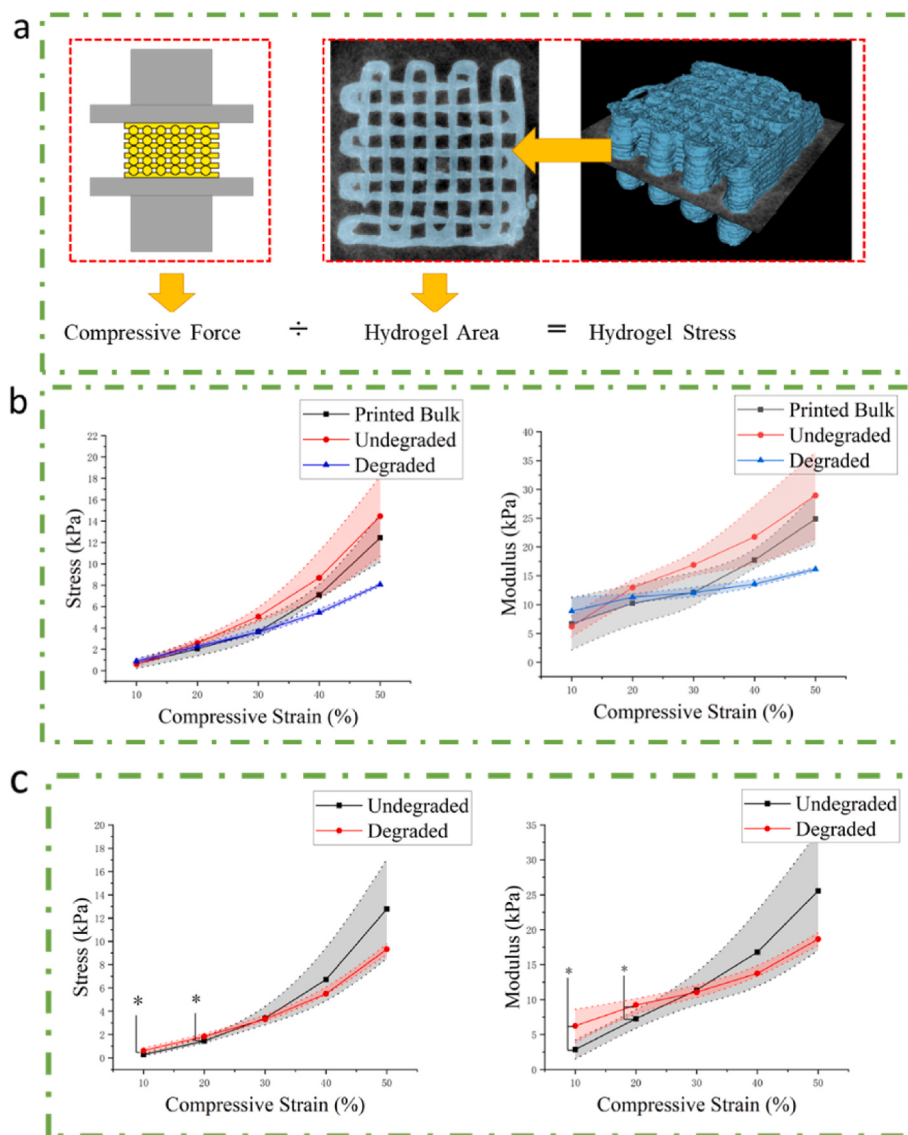


Fig. 16. Average stress in hydrogel of both undegraded and degraded scaffolds. Calculation scheme of average central hydrogel stress (a). Calculated average stress and modulus in hydrogel during compression using imaging data, with printed undegraded bulk sample (b). Calculated stress and modulus of degraded and undegraded scaffolds without imaging data ($n = 4$) (c). *, $p < 0.05$.

leading to a smaller stress and modulus comparing with actual values. The similarity demonstrated the precision of this combined method to access the stress within the hydrogel of the scaffolds.

Following this method, the average stress within the hydrogel of undegraded and degraded scaffolds was available. This comprehensive analysis provides valuable insights into the mechanical behavior and performance of the scaffolds, contributing to the understanding of their potential applications in various fields, such as tissue engineering and regenerative medicine.

4. Conclusions

Non-invasive characterization of 3D hydrogel scaffolds is critical for facilitating longitudinal studies on tissue engineering scaffolds. In this research, a novel method to characterize the mechanical properties of hydrogel scaffolds was developed using SR-PBI-CT imaging. The loading strategy of compression testing was modified to determine the stress of hydrogel scaffolds in mechanical environments during visualization; then 3D volume data from SR-PBI-CT imaging was analyzed for the detailed internal architecture of scaffolds; finally, the combination of the

result from the compression test and SR-PBI-CT imaging provided the further characterization of mechanical properties of scaffolds with precision in mechanical environment.

First, developed compression tests successfully determined the relaxed stress of hydrogel scaffolds in mechanical environments during visualization. The modified strain-time loading strategy can ensure the mechanical environment of scaffolds was consistent in this study, and typical stress-time curves showing viscoelastic properties of hydrogel were obtained. With the mechanical reaction of scaffolds under a specific mechanical environment recorded, the relaxed stress was obtained as applied stress for future analysis, with the range around 5–25 kPa. Two groups of samples showed significantly different results within the 20% range of compressive strain.

Then 3D imaging data from SR-PBI-CT can be used to evaluate the internal architecture of scaffolds. The structure stability, geometry change of strands, and changes in the properties of pore were successfully characterized using reconstructed 3D data.

Finally, the combination of the results from the compression test and SR-PBI-CT imaging can provide the further characterization of the mechanical properties of scaffolds in the mechanical environment with

verified precision. The stress in hydrogel material was calculated with the compressive force and hydrogel cross-sectional area, determined average max stress as 14 kPa for undegraded scaffolds and 8 kPa for degraded scaffolds. Furthermore, the precision of the method has been successfully verified by comparing the results of undegraded scaffolds and conventional tested undegraded printed bulk.

This research reveals the great potential of applying SR-PBI-CT to visualize and characterize the mechanical properties and microstructures of biodegradable hydrogel scaffolds non-invasively for tissue engineering. This is a significant advancement towards longitudinal studies of the tissue engineering scaffolds, once implanted in animal models or human patients with more complicated mechanical environments.

CRediT authorship contribution statement

Naitao Li: Writing – review & editing, Writing – original draft, Visualization, Validation, Software, Resources, Project administration, Methodology, Investigation, Formal analysis, Data curation, Conceptualization. **Xiaoman Duan:** Data curation. **Xiao Fan Ding:** Software. **Ning Zhu:** Supervision, Funding acquisition, Conceptualization. **Xiongbiao Chen:** Supervision, Funding acquisition, Conceptualization.

Declaration of competing interest

The authors declare that they have no known competing financial interests or personal relationships that could have appeared to influence the work reported in this paper.

Acknowledgements

It is acknowledged that this study was supported by the Natural Sciences and Engineering Research Council of Canada (NSERC; RGPIN 06007-2019 and RGPIN 06396-2019). Imaging, reconstruction, and segmentation parts of this research were performed at the Canadian Light Source, which is a national research facility supported by the Canada Foundation for Innovation (CFI), NSERC, National Research Council (NRC), Canadian Institutes of Health Research (CIHR), Government of Saskatchewan, and the University of Saskatchewan.

Data availability

Data will be made available on request.

References

- Cheah, C., Chua, C., Leong, K., Chua, S., 2003. Development of a tissue engineering scaffold structure library for rapid prototyping. Part 1: investigation and classification. *Int. J. Adv. Des. Manuf. Technol.* 21, 291–301. <https://doi.org/10.1007/s001700300034>, 10.1007/s001700300034.
- Chen, D.X., 2019. *Extrusion Bioprinting Of Scaffolds* (Extrusion Bioprinting of Scaffolds for Tissue Engineering Applications). Springer. <https://doi.org/10.1007/978-3-030-03460-3>.
- Clark, J.N., et al., 2020. Exploratory full-field mechanical analysis across the osteochondral tissue-biomaterial interface in an ovine model. *Materials (Basel)* 13 (18), 3911. <https://doi.org/10.3390/ma13183911>, 10.3390/ma13183911.
- Cox, T.R., Erler, J.T., 2011. Remodeling and homeostasis of the extracellular matrix: implications for fibrotic diseases and cancer. *Dis. Model Mech.* 4 (2), 165–178. <https://doi.org/10.1242/dmm.004077>, 10.1242/dmm.004077.
- Derby, B., 2012. Printing and prototyping of tissues and scaffolds. *Science* 338 (6109), 921–926. <https://doi.org/10.1126/science.1226340>, 10.1126/science.1226340.
- Discher, D.E., Janmey, P., Wang, Y.-l., 2005. Tissue cells feel and respond to the stiffness of their substrate. *Science* 310 (5751), 1139–1143. <https://doi.org/10.1126/science.1116995>, 10.1126/science.1116995.
- Duan, X., Li, N., Chen, X., Zhu, N., 2021. Characterization of tissue scaffolds using synchrotron radiation microcomputed tomography imaging. *Tissue Eng. C Methods* 27 (11), 573–588. <https://doi.org/10.1089/ten.TEC.2021.0155>, 10.1089/ten.TEC.2021.0155.
- Farago, T., et al., 2022. Tofu: a fast, versatile and user-friendly image processing toolkit for computed tomography. *J. Synchrotron Radiat.* 29 (Pt 3), 916–927. <https://doi.org/10.1107/S160057752200282X>, 10.1107/S160057752200282X.
- Gong, J.P., 2010. Why are double network hydrogels so tough? *Soft Matter* 6 (12), 2583–2590. <https://doi.org/10.1039/b924290b>, 10.1039/b924290b.
- Handorf, A.M., Zhou, Y., Halanski, M.A., Li, W.J., 2015. Tissue stiffness dictates development, homeostasis, and disease progression. *Organogenesis* 11 (1), 1–15. <https://doi.org/10.1080/15476278.2015.1019687>, 10.1080/15476278.2015.1019687.
- Hennink, W.E., van Nostrum, C.F., 2012. Novel crosslinking methods to design hydrogels. *Adv. Drug Deliv. Rev.* 64, 223–236. <https://doi.org/10.1016/j.addr.2012.09.009>, 10.1016/j.addr.2012.09.009.
- Hollister, S.J., 2005. Porous scaffold design for tissue engineering. *Nat. Mater.* 4 (7), 518–524. <https://doi.org/10.1038/nmat1421>, 10.1038/nmat1421.
- Izadifar, Z., Honaramooz, A., Wiebe, S., Belev, G., Chen, X., Chapman, D., 2016. Low-dose phase-based X-ray imaging techniques for *in situ* soft tissue engineering assessments. *Biomaterials* 82, 151–167. <https://doi.org/10.1016/j.biomaterials.2015.11.044>, 10.1016/j.biomaterials.2015.11.044.
- Jang, J.-W., Min, K.-E., Kim, C., Shin, J., Lee, J., Yi, S., 2023. Review: scaffold characteristics, fabrication methods, and biomaterials for the bone tissue engineering. *Int. J. Precis. Eng. Manuf.* 24 (3), 511–529. <https://doi.org/10.1007/s12541-022-00755-7>, 10.1007/s12541-022-00755-7.
- Karageorgiou, V., Kaplan, D., 2005. Porosity of 3D biomaterial scaffolds and osteogenesis. *Biomaterials* 26 (27), 5474–5491. <https://doi.org/10.1016/j.biomaterials.2005.02.002>, 10.1016/j.biomaterials.2005.02.002.
- Kikinis, R., Pieper, S.D., Vosburgh, K.G., 2014. 3D Slicer: a platform for subject-specific image analysis, visualization, and clinical support. In: *Intraoperative Imaging and Image-Guided Therapy*. Springer, pp. 277–289. https://doi.org/10.1007/978-1-4614-7657-3_19.
- Kim, Y.B., Van Le, T., Lee, J.Y., 2024. Lightweight brain MR image super-resolution using 3D convolution. *Medical Tool. Appl.* 83 (3), 8785–8795. <https://doi.org/10.1007/s11042-023-15969-8>, 10.1007/s11042-023-15969-8.
- Larson, C., Shepherd, R., 2016. 3D bioprinting technologies for cellular engineering. In: *Microscale Technologies for Cell Engineering*. Springer, pp. 69–89. https://doi.org/10.1007/978-3-319-20726-1_4.
- Lei, I.M., et al., 2021. 3D printed biomimetic cochlea and machine learning co-modelling provides clinical informatics for cochlear implant patients. *Nat. Commun.* 12 (1), 6260. <https://doi.org/10.1038/s41467-021-26491-6>, 10.1038/s41467-021-26491-6.
- Lewis, R.A., 2004. Medical phase contrast x-ray imaging: current status and future prospects. *Phys. Med. Biol.* 49 (16), 3573–3583. <https://doi.org/10.1088/0031-9155/49/16/005>, 10.1088/0031-9155/49/16/005.
- Loh, Q.L., Choong, C., 2013. Three-dimensional scaffolds for tissue engineering applications: role of porosity and pore size. *Tissue Eng., Part B* 19 (6), 485–502. <https://doi.org/10.1089/ten.TEB.2012.0437>, 10.1089/ten.TEB.2012.0437.
- Lösel, P.D., et al., 2020. Introducing Biomedisa as an open-source online platform for biomedical image segmentation. *Nat. Commun.* 11 (1), 5577. <https://doi.org/10.1038/s41467-020-19303-w>, 10.1038/s41467-020-19303-w.
- Lu, H.H., Thomopoulos, S., 2013. Functional attachment of soft tissues to bone: development, healing, and tissue engineering. *Annu. Rev. Biomater. Eng.* 15, 201–226. <https://doi.org/10.1146/annurev-bioeng-071910-124656>, 10.1146/annurev-bioeng-071910-124656.
- Luo, Y., Zhang, T., Lin, X., 2022. 3D printed hydrogel scaffolds with macro pores and interconnected microchannel networks for tissue engineering vascularization. *Chem. Eng. J.* 430, 132926. <https://doi.org/10.1016/j.cej.2021.132926>, 10.1016/j.cej.2021.132926.
- Ma, P.X., 2004. Scaffolds for tissue fabrication. *Mater. Today* 7 (5), 30–40. [https://doi.org/10.1016/S1369-7021\(04\)00233-0](https://doi.org/10.1016/S1369-7021(04)00233-0), 10.1016/S1369-7021(04)00233-0.
- Martino, M.M., et al., 2014. Growth factors engineered for super-affinity to the extracellular matrix enhance tissue healing. *Science* 343 (6173), 885–888. <https://doi.org/10.1126/science.1247663>, 10.1126/science.1247663.
- Metcalf, C.D., et al., 2020. Quantifying soft tissue artefacts and imaging variability in motion capture of the fingers. *Ann. Biomed. Eng.* 48 (5), 1551–1561. <https://doi.org/10.1007/s10439-020-02476-2>, 10.1007/s10439-020-02476-2.
- Naahidi, S., et al., 2017. Biocompatibility of hydrogel-based scaffolds for tissue engineering applications. *Biotechnol. Adv.* 35 (5), 530–544. <https://doi.org/10.1016/j.biotechadv.2017.05.006>, 10.1016/j.biotechadv.2017.05.006.
- Naghieh, S., Karamooz-Ravari, M.R., Sarker, M.D., Karki, E., Chen, X., 2018a. Influence of crosslinking on the mechanical behavior of 3D printed alginate scaffolds: experimental and numerical approaches. *J. Mech. Behav. Biomed. Mater.* 80, 111–118. <https://doi.org/10.1016/j.jmbbm.2018.01.034>, 10.1016/j.jmbbm.2018.01.034.
- Naghieh, S., Karamooz-Ravari, M.R., McInnes, A.D., Chen, X., 2018b. Modeling of the mechanical behavior of 3D bioplotted scaffolds considering the penetration in interlocked strands. *Appl. Sci.* 8 (9), 1422. <https://doi.org/10.3390/app8091422>, 10.3390/app8091422.
- Naghieh, S., Sarker, M.D., Abelseth, E., Chen, X., 2019a. Indirect 3D bioprinting and characterization of alginate scaffolds for potential nerve tissue engineering applications. *J. Mech. Behav. Biomed. Mater.* 93, 183–193. <https://doi.org/10.1016/j.jmbbm.2019.02.014>, 10.1016/j.jmbbm.2019.02.014.
- Naghieh, S., Sarker, M., Sharma, N., Barhoumi, Z., Chen, X., 2019b. Printability of 3D printed hydrogel scaffolds: influence of hydrogel composition and printing parameters. *Appl. Sci.* 10 (1), 292. <https://doi.org/10.3390/app10010292>, 10.3390/app10010292.
- Ning, L., et al., 2021. Noninvasive three-dimensional *in situ* and *in vivo* characterization of bioprinted hydrogel scaffolds using the X-ray propagation-based imaging technique. *ACS Appl. Mater. Interfaces* 13 (22), 25611–25623. <https://doi.org/10.1021/acsami.1c02297>, 10.1021/acsami.1c02297.

- Paganin, D., Mayo, S.C., Gureyev, T.E., Miller, P.R., Wilkins, S.W., 2002. Simultaneous phase and amplitude extraction from a single defocused image of a homogeneous object. *J. Microsc.* 206 (Pt 1), 33–40. <https://doi.org/10.1046/j.1365-2818.2002.01010.x>.
- Radulescu, D.M., Neacsu, I.A., Grumezescu, A.M., Andronescu, E., 2022. New insights of scaffolds based on hydrogels in tissue engineering. *Polymers (Basel)* 14 (4), 799. <https://doi.org/10.3390/polym14040799>, 10.3390/polym14040799.
- Rawson, S.D., Maksimcuka, J., Withers, P.J., Cartmell, S.H., 2020. X-ray computed tomography in life sciences. *BMC Biol.* 18 (1), 21. <https://doi.org/10.1186/s12915-020-0753-2>, 10.1186/s12915-020-0753-2.
- Saroiu, J., Yanen, W., Wei, Q., Zhang, K., Lu, T., Zhang, B., 2018. A review on biocompatibility nature of hydrogels with 3D printing techniques, tissue engineering application and its future prospective. *Bio-Des. Manufact.* 1, 265–279. <https://doi.org/10.1007/s42242-018-0029-7>, 10.1007/s42242-018-0029-7.
- Schneider, C.A., Rasband, W.S., Eliceiri, K.W., 2012. NIH Image to ImageJ: 25 years of image analysis. *Nat. Methods* 9 (7), 671–675. <https://doi.org/10.1038/nmeth.2089>, 10.1038/nmeth.2089.
- Shimojo, A.A.M., Rodrigues, I.C.P., Perez, A.G.M., Souto, E.M.B., Gabriel, L.P., Webster, T., 2020. Scaffolds for tissue engineering: a state-of-the-art review concerning types, properties, materials, processing, and characterization. Racing for the surface: Antimicrobial and Interface tissue engineering 647–676. https://doi.org/10.1007/978-3-030-34471-9_23, 10.1007/978-3-030-34471-9_23.
- Singh, B.K., Sirohi, R., Archana, D., Jain, A., Dutta, P., 2015. Porous chitosan scaffolds: a systematic study for choice of crosslinker and growth factor incorporation. *Int. J. Polym. Mater. Biomater.* 64 (5), 242–252. <https://doi.org/10.1080/00914037.2014.936596>.
- Stucht, D., Danishad, K.A., Schulze, P., Godenschweger, F., Zaitsev, M., Speck, O., 2015. Highest resolution in vivo human brain MRI using prospective motion correction. *PLoS One* 10 (7), e0133921. <https://doi.org/10.1371/journal.pone.0133921>, 10.1371/journal.pone.0133921.
- Szulc, D.A., Ahmadipour, M., Aoki, F.G., Waddell, T.K., Karoubi, G., Cheng, H.M., 2020. MRI method for labeling and imaging decellularized extracellular matrix scaffolds for tissue engineering. *Magn. Reson. Med.* 83 (6), 2138–2149. <https://doi.org/10.1002/mrm.28072>, 10.1002/mrm.28072.
- Tibbitt, M.W., Anseth, K.S., 2009. Hydrogels as extracellular matrix mimics for 3D cell culture. *Biotechnol. Bioeng.* 103 (4), 655–663. <https://doi.org/10.1002/bit.22361>, 10.1002/bit.22361.
- Zadpoor, A.A., 2019. Mechanical performance of additively manufactured meta-biomaterials. *Acta Biomater.* 85, 41–59. <https://doi.org/10.1016/j.actbio.2018.12.038>.
- Zhang, Y.S., Khademhosseini, A., 2017. Advances in engineering hydrogels. *Science* 356 (6337), eaaf3627. <https://doi.org/10.1126/science.aaf3627>, 10.1126/science.aaf3627.
- Zhao, P., Gu, H., Mi, H., Rao, C., Fu, J., Turng, L.-s., 2018. Fabrication of scaffolds in tissue engineering: a review. *Front. Mech. Eng.* 13 (1), 107–119. <https://doi.org/10.1007/s11465-018-0496-8>, 10.1007/s11465-018-0496-8.